Physics of Fluids

RESEARCH ARTICLE | SEPTEMBER 15 2022

# New phase diagram of miscible viscous fingering instabilities in porous media with dead-end pores

Qingwang Yuan (苑庆旺) ; Bowen Ling (凌博闻) ; Saman A. Aryana

Check for updates

*Physics of Fluids* 34, 092109 (2022)
https://doi.org/10.1063/5.0104692

CrossMark

View Online Export Citation

Articles You May Be Interested In

Viscous fingering of miscible slices
*Physics of Fluids* (May 2005)

Miscible viscous fingering in microgravity
*Physics of Fluids* (May 2009)

Fingering regimes in unstable miscible displacements
*Physics of Fluids* (January 2020)

Physics of Fluids
Special Topic: Flow and Forensics
Submit Today!
AIP Publishing

AIP Publishing

Downloaded from http://pubs.aip.org/aip/pof/article-pdf/doi/10.1063/5.0104692/16569127/092109_1_online.pdf

Physics of Fluids ARTICLE scitation.org/journal/phf

# New phase diagram of miscible viscous fingering instabilities in porous media with dead-end pores

Cite as: Phys. Fluids **34**, 092109 (2022); doi: 10.1063/5.0104692
Submitted: 20 June 2022 · Accepted: 23 August 2022 ·
Published Online: 15 September 2022

View Online Export Citation CrossMark

Qingwang Yuan (苑庆旺),[1,a)] Bowen Ling (凌博闻),[2,a)] and Saman A. Aryana[3]

## AFFILIATIONS

[1]Bob L. Herd Department of Petroleum Engineering, Texas Tech University, Lubbock, Texas 79409, USA
[2]Institute of Mechanics, Chinese Academy of Sciences, Beijing 100190, China
[3]Department of Chemical Engineering, University of Wyoming, Laramie, Wyoming 82071, USA

[a)]**Authors to whom correspondence should be addressed:** Qingwang.Yuan@ttu.edu and lingbowen@imech.ac.cn

## ABSTRACT

Classical miscible viscous fingering (VF) instability occurs when a less viscous fluid displaces a more viscous one in porous media with pores that are all well connected. Here, we investigate numerically how non-negligible dead-end pores, together with a limited mass transfer rate *Da* between the two pore types, affect fingering dynamics. We identify a new stabilizing mechanism induced by a reduction of effective viscosity contrast at an intermediate *Da*, which leads to a new phase diagram for VF instabilities in a Péclet number—*Pe*–*Da* parameter space and an elimination of fingers and tip-splitting at low and large values of *Pe*, respectively. A scaling analysis, along with an analysis of interfacial lengths, accurately predicts the boundary of the flow regimes and explains the origin of the new stabilizing mechanism.

*Published under an exclusive license by AIP Publishing.* https://doi.org/10.1063/5.0104692

## I. INTRODUCTION

Fluid flow instabilities in miscible displacements are of particular interest in many applications such as chromatographic separation,[1] diagnosis of cancer,[2] carbon dioxide ($CO_2$) sequestration,[3] hydrogen geologic storage,[4] subsurface water remediation,[5] enhanced oil recovery,[6] among others. Such instabilities are often referred to as viscous fingering (VF), a dynamic finger-like pattern that is formed when a less viscous fluid displaces a more viscous one.[7] In the literature, VF is often expected to happen under a certain viscosity contrast in either a simple Hele–Shaw cell or homogeneous, or a heterogeneous porous medium[8–11] and the resident fluid is almost completely displaced from the swept regions. This classical viewpoint is challenged when non-negligible dead-end pores, which are ubiquitous in natural and engineered systems, are present. To the best of our knowledge, this is the first time the effect of dead-end pores on VF is investigated systematically.

While previous studies on VF have *implicitly* assumed all pores in porous media are well connected,[7,9,12,13] the stagnant volumes, or the so-called dead-end pores, are, however, widely distributed in a variety of porous media such as coals,[14,15] geological rocks,[16–18] extracellular matrix in the brain,[2,19,20] batteries,[21,22] catalyst layers in fuel cells,[23] and filtration membranes.[24] Fluid flows and displacements in such porous media differ considerably from well-connected media, which are characterized by fluid transport that is governed by convection and diffusion. Specifically, the trapped fluids in dead-end pores are inaccessible to convection but may act as a source that slowly diffuses matter into adjacent well-connected pores.[3,25–27] The influence of such local mass transfer between the two pore types, coupled with macroscopic convection–diffusion in well-connected pore network, on VF instabilities and flow regimes remains unknown.

In this work, we characterize the miscible VF dynamics through nonlinear numerical simulations. We show that under unfavorable viscosity contrasts, the commonly encountered VF instabilities at a lower Péclet number (*Pe*) and tip-splitting at a large *Pe* are completely eliminated by an intermediate mass transfer rate between the two pore types, and that this phenomenon may be represented by the Damköhler number (*Da*). This introduces a new stabilizing mechanism that can greatly suppress VF instabilities, regardless of the value of *Pe*. We present a new phase diagram in terms of VF instabilities in a *Pe*–*Da* parameter space and delineate flow regimes. We use a scaling analysis to distinguish various flow regimes as a function of *Pe*, *Da*, and the proportion of dead-end pores. Finally, we discuss the origin of the new stabilizing mechanism and the implication of this work in complex VF structures and interfacial lengths.

## II. EQUATIONS AND NUMERICAL METHODS

We consider a two-dimensional (2D) homogeneous porous medium with uniformly distributed well-connected pores (volume

Downloaded from http://pubs.aip.org/aip/pof/article-pdf/doi/10.1063/5.0104692/16569127/092109_1_online.pdf


Published under an exclusive license by AIP Publishing

fraction, $f$), dead-end pores (volume fraction, $1-f$), and a constant overall porosity ($\phi$). A solvent with higher viscosity $\hat{\mu}_2$ initially saturates all the pore space and is displaced miscibly by a less viscous fluid with a viscosity of $\hat{\mu}_1$ under a constant injection rate of $\hat{U}_0$. Both fluids are assumed to be incompressible. The mixing of fluids in a well-connected pore network is determined by convection and a constant diffusivity $\hat{D}$. The mass transfer of fluids between two pore types is assumed to be governed by a rate coefficient $\hat{\alpha}$ and the concentration difference in and out of the dead-end pores, that is, the first-order mass transfer model.[25] The miscible displacements take place in a horizontal porous medium with a constant permeability $k$ and a fixed aspect ratio $A = l/w = 2$, where $l$ and $w$ are length and width of the domain, respectively. The dimensional equations are given

$$\hat{\nabla}\cdot\hat{\mathbf{u}} = 0, \tag{1a}$$

$$\hat{\nabla}\hat{p} = -\frac{\hat{\mu}_m}{\hat{k}}\hat{\mathbf{u}}, \tag{1b}$$

$$f\frac{\partial \hat{c}_m}{\partial \hat{t}} + \hat{\alpha}(1-f)(\hat{c}_m - \hat{c}_{im}) + \hat{\mathbf{u}}\cdot\hat{\nabla}\hat{c}_m = \hat{D}\hat{\nabla}^2\hat{c}_m, \tag{1c}$$

$$\frac{\partial \hat{c}_{im}}{\partial \hat{t}} = \hat{\alpha}(\hat{c}_m - \hat{c}_{im}), \tag{1d}$$

where the $(\hat{\cdot})$ indicates that the variable is dimensional. $\hat{\nabla}$ is dimensional differentiation operator, $\hat{\mathbf{u}}$ is the 2D Darcy velocity $\hat{\mathbf{u}} = (\hat{u}, \hat{v})$, $\hat{p}$ is pressure, $\hat{\mu}$ is viscosity, $\hat{k}$ is permeability, $\hat{c}$ is concentration, and $\hat{t}$ is time. Subscripts $m$ and $im$ represent the fluids in well-connected and dead-end pore networks, which are also referred to mobile and immobile fluids, respectively.[25,28] The overall concentration in any control volume is therefore $\hat{c}_T = f\hat{c}_m + (1-f)\hat{c}_{im}$. The permeability $\hat{k}$ is assumed to be independent of $f$ as indicated in previous work.[29] For simplicity, the term $\hat{\mu}_m/\hat{k}$ is written as $\hat{\mu}_m$. We then choose the characteristic variables as

$$L = \hat{D}\phi/\hat{U}_0, \quad U = \hat{U}_0/\phi, \quad T = \hat{D}\phi^2/\hat{U}_0{}^2, \quad P = \hat{\mu}_2\hat{D}\phi/\hat{k}, \tag{2}$$

where $L$, $U$, $T$, and $P$ are the scales for space, velocity, time, and pressure, respectively. $\hat{U}_0$ is a constant injection rate. More details for choosing characteristic variables and non-dimensionalizing equations can be found in previous studies.[7,30,31] The governing equations in dimensionless form in a fixed reference frame are

$$\nabla\cdot\mathbf{u} = 0, \tag{3a}$$

$$\nabla p = -\mu_m\mathbf{u}, \tag{3b}$$

$$f\frac{\partial c_m}{\partial t} + Da(1-f)(c_m - c_{im}) + \mathbf{u}\cdot\nabla c_m = \nabla^2 c_m, \tag{3c}$$

$$\frac{\partial c_{im}}{\partial t} = Da(c_m - c_{im}). \tag{3d}$$

$Da = \hat{\alpha}\hat{D}\phi^2/\hat{U}_0^2$ is the Damköhler number, which is the ratio of mass transfer rate between two pore types to the convection rate.[32] Note that $Da$ here is different from that used in reactive flows and wormhole development.[13,33] Equation (3c) is a non-Fickian convection–diffusion model with a source term (the second term) representing mass transfer between the two pore types.

An exponential concentration–viscosity relation is given for the fluid mixture in the well-connected pore network, $\mu_m(c_m) = e^{Rc_m}$, where $R = \ln(\mu_{m2}/\mu_{m1})$ is the log-viscosity ratio. Based on diffusive scaling [Eq. (2)], the dimensionless length and width of the domain are represented by the Péclet number $Pe = \hat{U}_0 l/(\hat{D}\phi)$ and $Pe/A$, respectively. An initial sharp interface between two fluids is located at the 1/64 of the domain, with small random perturbations on the interface.[31] A periodic boundary condition is assumed in the transverse direction of fluid flows. A streamfunction–vorticity formulation is employed with $(u, v) = (1 + \frac{\partial\psi}{\partial y}, -\frac{\partial\psi}{\partial x})$ and $\omega = -\nabla^2\psi$, where the $\frac{\partial\psi}{\partial y}$ is a velocity perturbation term. Equation (3a) is automatically met, while the Eqs. (3b) and (3c) become

$$\omega = R\left[\frac{\partial\psi}{\partial x}\frac{\partial c_m}{\partial x} + \left(\frac{\partial\psi}{\partial y} + 1\right)\frac{\partial c_m}{\partial y}\right], \tag{4a}$$

$$f\frac{\partial c_m}{\partial t} + Da(1-f)(c_m - c_{im}) + \left(1 + \frac{\partial\psi}{\partial y}\right)\frac{\partial c_m}{\partial x} - \frac{\partial\psi}{\partial x}\frac{\partial c_m}{\partial y} = \nabla^2 c_m. \tag{4b}$$

We solve the governing equations in a fixed reference frame, instead of the widely used moving reference frame.[7] For the time advancement, we employ a second-order, fully implicit, alternating-direction implicit (ADI) method.[34] The spatial derivatives in $x$ and $y$ directions are calculated by the sixth-order compact finite difference method[35] and fast Hartley Transform,[36] respectively. The code has been validated and proven to be robust at $Pe$ as high as 10 000 at $R = 3$.

The VF dynamics are determined by $R$, $Pe$, $Da$, and $f$. The ranges of the physical parameters, such as $f$, porosity, mass transfer rate between two pore types, flow velocity, diffusion or dispersion coefficient, fluid system, and porous media types, are given in Appendix A. Particularly, $f$ is typically larger than 0.5 for various porous media.[3,25,37–39] $Pe$ is larger than 100 based on the diffusive scaling and the chosen characteristic variables.[11,40–46] $Da$ varies several orders of magnitude depending on the properties of fluids and porous media, flow rate, and mass transfer rate between two pore types.[3,37,38,47] A range of $Da \in [0.0001, 1.0]$ is used in this work as our numerical simulations show that the viscous fingering dynamics is insensitive to $Da$ when it is too small (i.e., less than 0.0001) or too large (i.e., larger than 1.0).

## III. RESULTS AND DISCUSSION

### A. New phase diagram of VF dynamics

When dead-end pores in porous media are considered, the flow dynamics and sweep efficiency differ from previous studies, which are based on the classical convection–diffusion equation. Our recent study shows that a substantial proportion of the resident fluid remains in the *swept area* in miscible displacements when the fluid retention in dead-end pores plays a role.[31] Fluids trapped in dead-end pores are not immediately accessible to the invading fluids. Instead, the dead-end pores act as a local source and exchange content with the adjacent well-connected pores driven by local concentration gradients. The unstable, non-uniform distribution of fluids in dead-end pores is induced by the VF dynamics in the well-connected pore network but lags behind due to the limited mass transfer rate between the two pore types. More details of the unique characteristics at fixed $f$, $Pe$, and $Da$ as well as a comparison with non-dead-end pore effect can be found in Yuan *et al.*[31]

In this work, we first investigate how the VF dynamics is affected when $Pe$ and $Da$ vary. To take advantage of the numerical simulations to identify the phase diagram in terms of VF instabilities, we assume that the physical parameters and $Pe$ and $Da$ are independent.

Downloaded from http://pubs.aip.org/aip/pof/article-pdf/doi/10.1063/5.0104692/16569127/092109_1_online.pdf


Published under an exclusive license by AIP Publishing

Although it is hard to keep them independent in reality, this provides an interesting perspective to develop the theory of unstable flows. Such simplification has been used for the wormhole dynamics during the dissolution of porous media.[48] Note that the *Da* there has a different meaning compared with the current work.

Figure 1 shows concentration fields, $c_T$, at breakthrough time for a wide spectrum of *Pe* and *Da* at $f = 0.6$ and $R = 3$. Similar concentration fields for $c_m$ in a well-connected pore network and $c_{im}$ in a dead-end pore network are shown in Figs. 6 and 7, respectively, in Appendix B. The most striking observation is that VF instabilities at lower *Pe* ($Pe < 1000$) and the tip-splitting at higher *Pe* ($Pe > 2000$) are completely eliminated at an intermediate $Da \in [0.005, 0.1]$. This result challenges the widely recognized viewpoint that the VF instabilities and tip-splitting are expected at certain *Pe* and unfavorable viscosity ratios, $R \sim 20$.[7,30,41,43] As *Da* varies, a non-monotonic change of VF instabilities is observed. The following regimes emerge from the examination of concentration fields in a *Pe*–*Da* parameter space: (i) stable regime (SR) at small *Pe* and intermediate *Da* values where VF cannot develop prior to breakthrough. In this regime, flow is dominated by diffusion in the well-connected pore network and mass transfer between the two pore types, but the latter mechanism plays a much stronger role in stabilizing the flows compared with the case of $f = 1.0$; (ii) tip-splitting regime (TR) at large *Pe* and either small or large *Da* values with strongly distorted patterns at finger tips; and (iii) channeling regime (CR) at other *Pe* and *Da* values where several major fingers dominate with little or no tip-splitting. Such non-monotonic behavior results from the change of the effective viscosity contrast in the well-connected pore network as *Da* varies. At small or large values of *Da*, more viscous fluids in dead-end pores diffuse out either too slow or too fast, leading to a sharp viscosity profile in well-connected pore network where convection promotes VF instabilities. At intermediate values of *Da*, the continuous diffusion of more-viscous fluids from dead-end pores may effectively increase the viscosity of the displacing fluids in swept area, which significantly reduces viscosity contrasts and stabilizes flows in the well-connected pore network. Several representative *y*-averaged viscosity profiles in the well-connected pore network are provided in Fig. 6. Different regimes are characterized by different degrees of smoothness, stiffness, and fluctuations of the viscosity profiles, while the profiles within each regime are qualitatively similar. Based on this analysis, it is concluded that the competition among convection, diffusion, and mass transfer between the two pore types determines the phase diagram in terms of VF instabilities in the *Pe*–*Da* parameter space. Figure 1 also reveals that the overall concentration of the remaining resident fluids in the swept area is noticeably higher at small *Da* values because of the slow mass transfer of trapped fluids in dead-end pores to well-connected pores. At larger values of *Da*, all resident fluids in the media are expected to be displaced. This phenomenon is shown with variations of *Da* in Fig. 7 in Appendix B.

We next examine the role of the dead-end pore volume on VF dynamics and the newly identified flow regimes. As illustrated in Figs. 2 and 8 (see Appendix B), as the fraction of dead-end pores decreases from 0.4 to 0.2 ($f$ from 0.6 to 0.8), the stable regime at low *Pe* shrinks while the tip-splitting regime expands at high *Pe*, which indicates that the stabilizing effect at the intermediate *Da* becomes weaker. This results from a diminished availability of higher-viscous fluids in dead-end pores to diffuse out and impact the effective viscosity contrast in the well-connected pore network. It is expected that the stabilizing effect vanishes as $f$ approaches 1.0. Figures 1 and 2 show that a decrease in the dead-end pore volume leads to two competing mechanisms: (i) a smaller dead-end pore volume means that more effective pore space is available to fluid flows, and thus, a later breakthrough is observed; and (ii) a smaller dead-end pore volume results in a weaker stabilizing effect and an earlier breakthrough. The competition between these two mechanisms results in a nontrivial breakthrough behavior.

## B. Scaling analysis

The interaction between $f$, *Pe*, and *Da* drives the resulting flow regimes and the non-monotonic behaviors of VF instabilities. Due to the non-symmetric behavior of the concentration base-state,[49] the

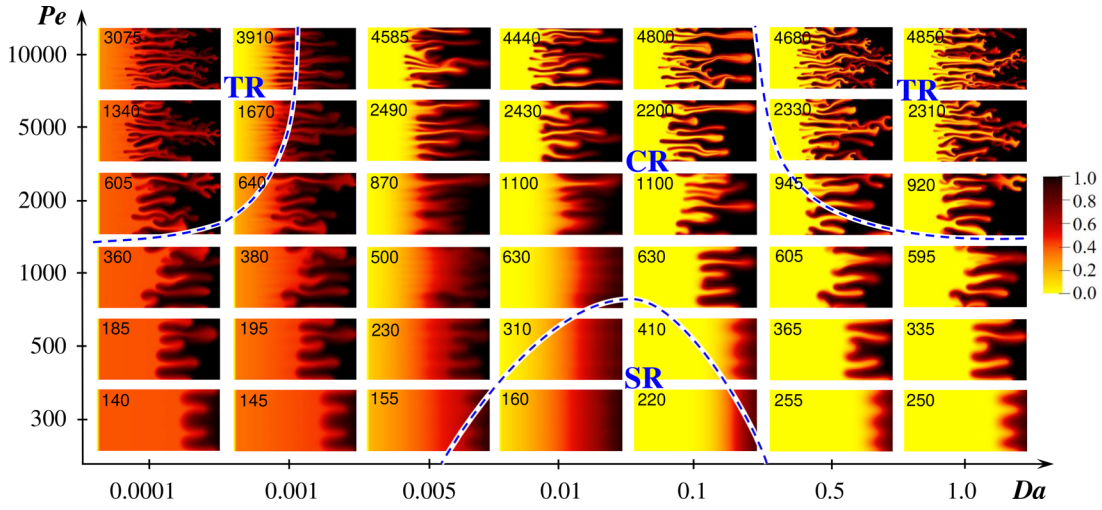


**FIG. 1.** Concentration fields $c_T$ in *Pe*–*Da* parameter space at $f = 0.6$ and $R = 3$. Dimensionless time is indicated at the left top corner of each frame. Flow regimes are identified as stable regime (SR), channeling regime without tip-splitting (CR), and tip-splitting regime (TR). Note the coordinate system is not to scale.

Downloaded from http://pubs.aip.org/aip/pof/article-pdf/doi/10.1063/5.0104692/16569127/092109_1_online.pdf


Published under an exclusive license by AIP Publishing

quasi-steady-state approximation (QSSA),[50] self-similar QSSA,[51] and non-modal analysis[52] are not applied as part of a linear stability analysis. Here, we conduct a scaling analysis based on convective scaling to examine the variations of the stable regime. The detailed formulation of variables and dimensional equations can be found in Appendix C. We assume that (i) mass transfer in and out of each dead-end pore is independent of other dead-end pores in any given control volume; and (ii) the change of concentration in adjacent well-connected pores is negligible within the observation time window. Based on these assumptions, the dimensional form of Eq. (3d) leads to the following ordinary differential equation:

$$\frac{dc_{im}}{dt} = \alpha T c_m - \alpha T c_{im}, \tag{5}$$

where $T$ is the characteristic time. We then impose an additional condition at the upstream direction of initial interface as

$$c_{im}|_{t=0} = 0. \tag{6}$$

The analytical solution is given as

$$c_{im} = (1 - e^{-\alpha T t}) c_m. \tag{7}$$

We then use $L$ and $U$ as the general scale notations for length and velocity, respectively, in the dimensional non-Fickian convection–diffusion model. Substituting Eq. (7) gives

$$f\frac{\partial c_m}{\partial t} + \alpha T(1-f)e^{-\alpha T t} c_m + \frac{UT}{\phi L}\mathbf{u}\cdot\nabla c_m = \frac{DT}{L^2}\nabla^2 c_m. \tag{8}$$

To obtain the criterion for the interfacial instability between low and high concentration zones, we examine one finger whose characteristic longitudinal and transverse lengths are $L_x$ and $L_y$. We estimate that the interface elongation along the longitudinal direction attributes mainly to advection, while the transverse length increment is due to diffusion. Namely, we have

$$\frac{UT}{\phi L} \sim \frac{UT}{\phi L_x}, \tag{9}$$

$$\frac{DT}{L^2} \sim \frac{DT}{L_y^2}, \tag{10}$$

and the expressions of $L_x$ and $L_y$ are obtained by balancing each of these two with the mass transfer term. We also consider that such balancing occurs within one diffusive characteristic timescale $T_{diff}$ (i.e., $T = T_{diff} = \frac{l^2}{D}$)—similar methodology is reported in the work by Panga *et al.*,[53]

$$Da(1-f)e^{-Da} \sim \frac{U_0 T_{diff}}{\phi L_x}, \tag{11a}$$

$$Da(1-f)e^{-Da} \sim \frac{DT_{diff}}{L_y^2}. \tag{11b}$$

To assess the stability of the interface, we define a length ratio $\Gamma$:

$$\Gamma = \frac{L_y}{L_x}. \tag{12}$$

It is clear that fingering occurs when $\Gamma \ll 1$ and the interface remains stable at $\Gamma \gg 1$. Substituting Eqs. (11a) and (11b) into $\Gamma$ gives

$$\Gamma = \sqrt{\frac{Da}{Pe^2}}(1-f)^{\frac{1}{2}} e^{-\frac{Da}{2}}. \tag{13}$$

A 3D plot of the variation of $\Gamma$ with $f$, $Pe$, and $Da$ is shown in Fig. 3. To match the actual $Da$–$Pe$ range, the values of $Pe$ and $Da$ are rescaled by 0.0002 and 10, respectively, in Eq. (13). As $f$ increases, the stable regime shrinks and finally disappears as $f$ approaches 1.0, as predicted by Eq. (13). This is consistent with the shrinkage of stable regime observed in Fig. 2.

### C. Origin of the stabilizing mechanism

When unstable flows are expected, the form of CR and TR regimes as well as the stabilizing mechanism may be well understood by a further examination of the variations of interfacial length and concentration contours with time. Interfacial length is calculated and normalized by its initial length, $\Psi(t) = \frac{\int_s \chi(\mathbf{x},t)ds}{\int_s \chi(\mathbf{x},t=0)ds}$, where the pseudo-interface $\chi(\mathbf{x}, t)$ is extracted from the concentration fields at a contour

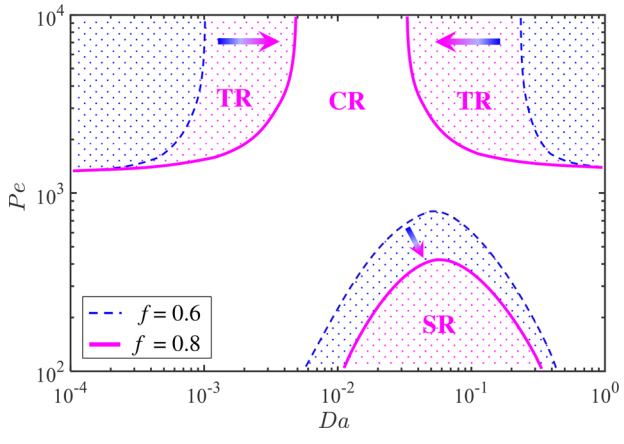


**FIG. 2.** Variations of phase diagrams (i.e., flow regimes) as $f$ increases from 0.6 to 0.8 (fraction of dead-end pore decreases from 0.4 to 0.2) at $R = 3$. The boundaries of flow regimes shift from blue ($f = 0.6$) to pink curves ($f = 0.8$).

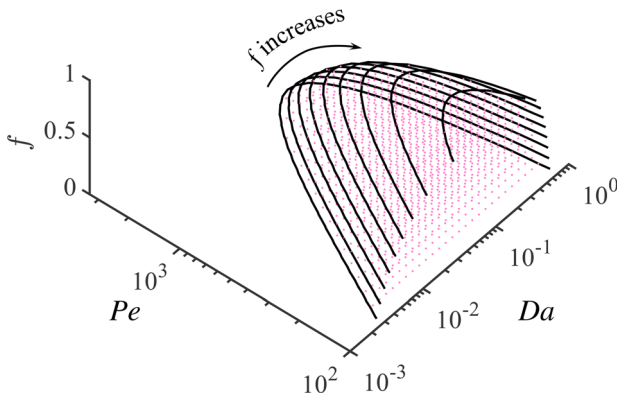


**FIG. 3.** Shrinkage of stable regime, that is, variations of $\Gamma$, when $f$ increases at $R = 3$.

Downloaded from http://pubs.aip.org/aip/pof/article-pdf/doi/10.1063/5.0104692/16569127/092109_1_online.pdf


Published under an exclusive license by AIP Publishing

$c_m = 0.1$ at time $t$. The MATLAB built-in function *imfill* is used to remove the isolated blobs of displaced fluid at large values of $Pe$ when coalescence of fingers happens frequently.[54] To ensure the same time-scale for different $Pe$, we normalize time by $Pe$ so that the convective time is $\frac{t}{Pe}$.

Figure 4 shows the variations of interfacial length and concentration contours from initial time to breakthrough at $Pe = 1000$ for different values of $Da$. For the cases with $f = 1.0$ or $f = 0.6$ and $Da \leq 0.001$ or $Da = 1.0$, the interfacial length exhibits a three-regime behavior: (1) regime I, the diffusion-dominated regime in which the flow is stable and interfacial length is nearly 1.0; (2) regime II where a number of small fingers grow quickly, thus the interfacial length increases fast with time; and (3) regime III where these smaller fingers coalesce and eventually several larger fingers are formed and dominate the flows.

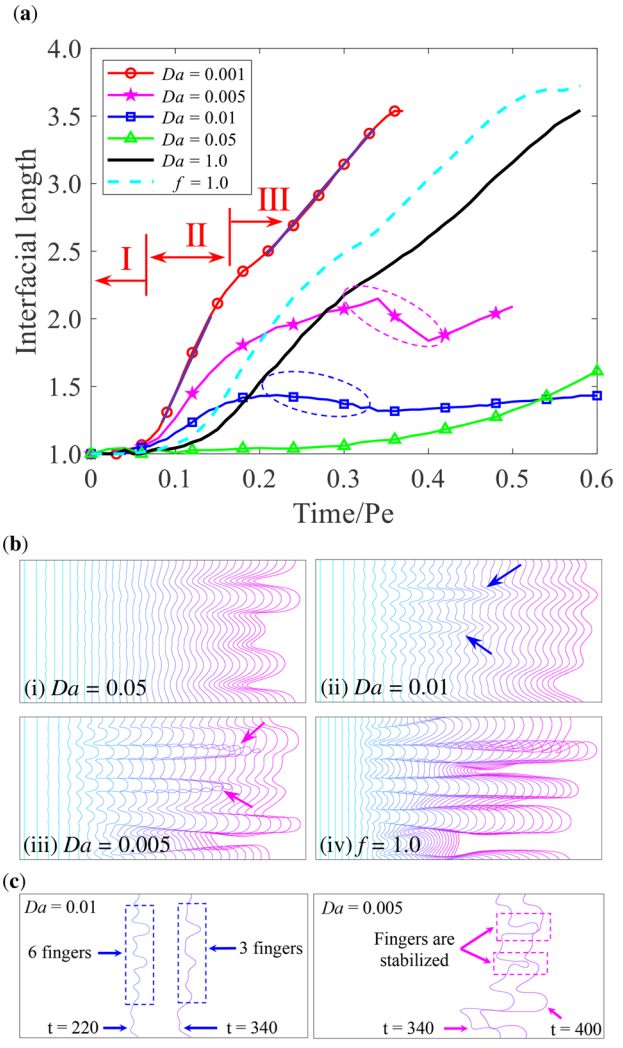


**FIG. 4.** Variations of interfacial length and concentration contours with time for $c_m$. (a) $f = 0.6$ and $f = 1.0$ at $Pe = 1000$ and different $Da$. (b) Concentration contours from initial time to breakthrough for $f = 0.6$ and $f = 1.0$ at $Pe = 1000$. (c) Stabilization of fingers depicted by concentration contours.

The slope of the interfacial length reflects how fast the fingers grow in each regime, which results from the competition among convection, diffusion in well-connected pore network, and diffusion between the two pore types. For instance, compared with $f = 1.0$, the steeper slope for the case $Da = 0.001$ results from the weaker stabilizing effect by the diffusion between the two pore types and the stronger convection due to the less available pore space at $f = 0.6$. In regimes II and III, the interfacial length grows linearly with time, but the slope of regime III is smaller due to the shielding of fingers; that is, larger fingers suppress their neighboring fingers.[54]

Note that the regimes I to III may be easily identified when the stabilizing effect is not strong for cases with $f = 1.0$ or $f = 0.6$ and $Da \leq 0.001$ or $Da \geq 1.0$. However, when the stabilizing effect becomes stronger, the behaviors of these three regimes are influenced significantly. The stabilizing mechanism is the strongest when, at a fixed $f$ and $Pe$, $Da$ is close to 0.05 and 0.01 in Fig. 4(a). At $Da = 0.05$, this stabilizing effect can significantly extend regime I by suppressing the initial development of fingering. As $Da$ increases from 0.05 to 1.0, the more viscous fluid tends to easily diffuse out of the dead-end pores, which increases the viscosity contrast of two fluids in well-connected pores. Thus, the flows become more unstable with a larger interfacial length and a shorter regime I. Meanwhile, as $Da$ decreases from 0.05 to 0.001, the more viscous fluid diffuses out more slowly from dead-end pores, thus requiring a longer time to reduce the effective viscosity contrast between the resident and displacing fluids in the swept area. Consequently, fingers tend to develop earlier and the interfacial length also tends to increase. Overall, the stabilizing mechanism leads to a non-monotonic behavior of interfacial length as $Da$ varies from 0.001 to 1.0. Such stabilizing mechanism not only suppresses the development of initial fingers but also mitigates the big fingers to some extent and results in the decrease in the interfacial length. More specifically, at $Da = 0.01$, six fingers are reduced to three from time $t = 220$ to $t = 340$ in Fig. 4(c), reflected by the smooth decrease in the interfacial length in Fig. 4(a) (blue dotted circle). Meanwhile, at $Da = 0.005$, even the big fingers are eliminated by the stabilizing mechanism, resulting in a sharp decrease in the interfacial length in Fig. 4(a) (pink circle). Note that the concentration contours at $Da = 0.01$ and 0.005, highlighted by the arrows in Fig. 4(b), indicate that there is no shielding or coalescence (i.e., pinch-off of fingers[54]) although they all lead to a decrease in the interfacial length. This distinguishes the new stabilizing mechanism in this work from the mechanisms reported previously in the literature.

Figure 5 indicates that the stabilizing effect varies with $Pe$ and $f$. As $Pe$ increases, convection becomes stronger; thus, the interfacial length increases faster. However, even when $Pe$ is as large as 10 000 at $f = 0.6$, the stabilizing effect still plays a role in mitigating fingering instability, which is clearly indicated by the smooth decrease in the interfacial length. In fact, the stabilizing effect lasts for the entire displacement process, while the mitigation of fingers, the decrease in the interfacial length, and the elimination of tip splitting are not noticeable. Eventually, convection dominates the flows at large values of $Pe$. This also explains channeling regime without tip splitting at $Pe \geq 2000$ and an intermediate $Da$ in Fig. 1. In addition, as the fraction of dead-end pores decreases, for example, $f$ changes from 0.6 to 0.8, the stabilizing mechanism becomes weaker. An evidence for this is that the mitigation of fingers and a decrease in the interfacial length can only be observed near breakthrough for $Da = 0.01$, $Pe = 1000$, and

Downloaded from http://pubs.aip.org/aip/pof/article-pdf/doi/10.1063/5.0104692/16569127/092109_1_online.pdf


Published under an exclusive license by AIP Publishing

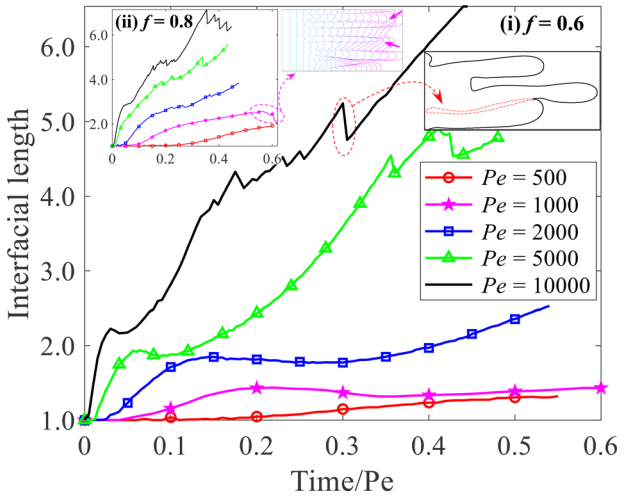


**FIG. 5.** Variations of interfacial length for $c_m$ with time at $f = 0.6$ and $f = 0.8$ for $Da = 0.01$ and different $Pe$.

$f = 0.8$. This is also consistent with the expansion of tip-splitting regime when $f$ increases from 0.6 to 0.8 in Figs. 2 and 8.

## IV. CONCLUSIONS

In summary, our study shows that the dead-end pores in porous media and local mass transfer between the two pore types profoundly affect VF dynamics and the remaining fluids in swept areas. Radically different from the traditional viewpoint, we demonstrate that the presence of dead-end pore volumes and slow mass transfer rates (i.e., small $Da$) lead to substantial unswept resident fluids in both well-connected and dead-end pores, making miscible displacements less efficient. Strikingly, we identify a new stabilizing mechanism that originates from the release of more viscous fluids from dead-end pores into well-connected pores. This stabilizing effect is only noticeable at intermediate $Da$ values and significantly suppresses the instabilities by completely eliminating both the VF phenomenon at low $Pe$ and tip-splitting at high $Pe$. A competition among convection, diffusion, and this new stabilizing mechanism leads to the non-monotonic behavior of VF dynamics as well as a new phase diagram in $Pe$–$Da$ parameter space for flow regimes including a stable regime, a channeling regime without tip-splitting, and a tip-splitting regime. As dead-end pore volume decreases, its stabilizing effect becomes weaker, leading to a shrinkage of the stable regime and an expansion of the tip-splitting regime. We further develop a simple model through scaling analysis that reveals the mechanisms for the stable regime and accurately predicts the boundary of this regime. We expect this work to contribute to a deeper understanding of the miscible VF dynamics in a variety of porous media with dead-end pores. Beyond these results, we envisage that this work will inspire exciting fundamental research in coupling the interesting and important physics in stagnant volume with the macroscopic flow dynamics in porous media in many applications.

## ACKNOWLEDGMENTS

Q.Y. thanks the Matejek Family Faculty Fellowship for financial support.

## AUTHOR DECLARATIONS

### Conflict of Interest

The authors have no conflicts to disclose.

### Author Contributions

**Qingwang Yuan:** Conceptualization (lead); Data curation (lead); Formal analysis (lead); Investigation (lead); Methodology (lead); Software (lead); Validation (lead); Visualization (lead); Writing – original draft (lead). **Bowen Ling:** Formal analysis (equal); Methodology (equal); Visualization (equal); Writing – review & editing (equal). **Saman Aryana:** Formal analysis (equal); Visualization (equal); Writing – review & editing (equal).

## DATA AVAILABILITY

The data that support the findings of this study are available from the corresponding authors upon reasonable request.

## APPENDIX A: RANGES OF PARAMETERS INVOLVED

The values of dimensionless numbers $Pe$ and $Da$ are determined by the physical parameters involved. The values of those physical parameters are obtained from the literature. The proportions of dead-end pores $(1 - f)$ and porosity for different porous media are shown in Table I. The ranges of mass transfer coefficient $\hat{\alpha}$ are given in Table II. The ranges of fluid flow velocity $U$ in different porous media are given in Table III. The ranges of diffusion/dispersion coefficient $D$ for different fluids are given in Table IV.

## APPENDIX B: VISCOUS FINGERING (VF) DYNAMICS

The VF dynamics in well-connected and dead-end pore network on the $Pe$–$Da$ parameter space are shown in Figs. 6 and 7,

**TABLE I.** Proportion of dead-end pores and porosity for different porous media.

| $1 - f$ (%) | Porosity (%) | Porous media type | Reference |
|---|---|---|---|
| <10.0 | 26.0–46.7 | Sandstone | 25 |
| 2.2–47.6 | 8.0–10.9 | Carbonate | 55 |
| 4.0–50.0 | 23.9 | Sandstone | 37 |
| 1.0–42.0 | 22.0–25.0 | Sandstone | 38 |
| 19.0–44.0 | 9.1–18.2 | Carbonate | 47 |
| 0.0–1.8 | 18.2–24.5 | Sandstone | 56 |
| 5.1–44.0 | 9.1–21.3 | Carbonate | 56 |
| 1.0–48.0 | 6.0–34.0 | Carbonate | 57 |
| 20.0 | 23.0 | Carbonate | 58 |
| 50.0 | 19.0 | Carbonate | 59 |
| 0.0–50.0 | 20.0 | Aquifer | 3 |
| <10.0 | 20.0 | Rock | 60 |
| <30.0 | … | Micromodel | 28 |
| 60.0 | … | Brain tissue | 61 |
| 7.5 | … | Battery | 21 |
| 32.8–72.6 | … | Muscles | 62 |

Downloaded from http://pubs.aip.org/aip/pof/article-pdf/doi/10.1063/5.0104692/16569127/092109_1_online.pdf


Published under an exclusive license by AIP Publishing

**TABLE II.** Ranges of mass transfer coefficient $\hat{\alpha}$ in different fluid flow systems.

| $\hat{\alpha}$ (1/s) | Fluid system | Reference |
|---|---|---|
| $(1.1 \times 10^{-9}, 3.6 \times 10^{-5})$ | Gas–gas | 55 |
| $(4.7 \times 10^{-6}, 4.0 \times 10^{-4})$ | Brine–oil | 38 |
| $(1.0 \times 10^{-7}, 3.6 \times 10^{-4})$ | Brine–tracer | 47 |
| $(1.0 \times 10^{-7}, 2.6 \times 10^{-5})$ | Brine–tracer | 56 |
| $(3.0 \times 10^{-6}, 1.0 \times 10^{-2})$ | Ink–water | 28 |
| $(1.0 \times 10^{-12}, 1.0 \times 10^{-4})$ | $CO_2$–brine | 3 |

**TABLE III.** Ranges of fluid flow velocity $U$ in different porous media.

| Velocity (m/s) | Reference |
|---|---|
| $(9.0 \times 10^{-5}, 2.5 \times 10^{-3})$ | 25 |
| $(2.54 \times 10^{-6}, 2.05 \times 10^{-3})$ | 55 |
| $(2.5 \times 10^{-6}, 3.9 \times 10^{-4})$ | 38 |
| $(2.6 \times 10^{-6}, 2.6 \times 10^{-4})$ | 47 |
| $(2.5 \times 10^{-5}, 4.3 \times 10^{-5})$ | 56 |
| $(2.9 \times 10^{-5}, 1.7 \times 10^{-4})$ | 57 |
| $(1.0 \times 10^{-8}, 6.0 \times 10^{-4})$ | 28 |
| $(1.0 \times 10^{-6}, 1.0 \times 10^{-5})$ | 63 |

respectively, for $f = 0.6$ and $R = 3$. The VF dynamics for $c_T$ in the *Pe*–*Da* parameter space are shown in Fig. 8 for $f = 0.8$ and $R = 3$.

## APPENDIX C: FORMULATION AND SCALING ANALYSIS

The governing equations in dimensional form for the miscible displacements in porous media with dead-end pores are given in Eqs. (1a)–(1d). We adopt general notations for the scaling analysis;

**TABLE IV.** Ranges of diffusion/dispersion coefficient $D$ for different fluids.

| $D$ ($m^2$/s) | Fluid system | Reference |
|---|---|---|
| $(4.5 \times 10^{-8}, 2.74 \times 10^{-6})$[a] | $CaCl_2$–NaCl solution | 25 |
| $O(1.4 \times 10^{-9})$[b] | NaCl in water | 25 |
| $(1.0 \times 10^{-9}, 1.0 \times 10^{-10})$[b] | Nonelectrolytes in dilute | 64 |
| $(1.5 \times 10^{-9}, 7.3 \times 10^{-9})$[b] | Brine–oil | 38 |
| $O(1.0 \times 10^{-9})$[b] | Brine–tracer | 47 |
| $(2.0 \times 10^{-7}, 5.0 \times 10^{-5})$[a] | Brine–tracer | 47 |
| $(5.6 \times 10^{-10}, 3.7 \times 10^{-9})$[b] | Toluene/heptane, sucrose/water | 32 |
| $(1.0 \times 10^{-9}, 3.0 \times 10^{-6})$[a] | Ink–water | 28 |
| $O(1.0 \times 10^{-8})$[b] | Oil–paraffinic solvent | 63 |
| $(6.0 \times 10^{-8}, 2.7 \times 10^{-7})$[b] | $CO_2$–brine | 65 |

[a]Dispersion coefficient.
[b]Diffusion coefficient.

specifically, we define $L$, $U$, $T$, $C$, and $P$ as the length, velocity, time, concentration, and pressure scales. Namely, variables and operators are written as

$$\nabla = L\hat{\nabla}, \quad \boldsymbol{u} = \frac{\hat{u}}{U}, \quad t = \frac{\hat{t}}{T}, \quad (c_m, c_{im}) = \frac{(\hat{c}_m, \hat{c}_{im})}{C}, \quad p = \frac{\hat{p}}{P}. \tag{C1}$$

Additionally, we use $\mu_m$ to represent $\frac{\mu_m}{k}$ for simplicity. The dimensionless equations based on the new scaling notations are, therefore,

$$\nabla \cdot \mathbf{u} = 0, \tag{C2a}$$

$$\nabla p = -\frac{\mu_m UL}{P}\mathbf{u}, \tag{C2b}$$

$$f\frac{\partial c_m}{\partial t} + \alpha T(1-f)(c_m - c_{im}) + \frac{UT}{\phi L}\boldsymbol{u}\cdot\nabla c_m = \frac{DT}{L^2}\nabla^2 c_m, \tag{C2c}$$

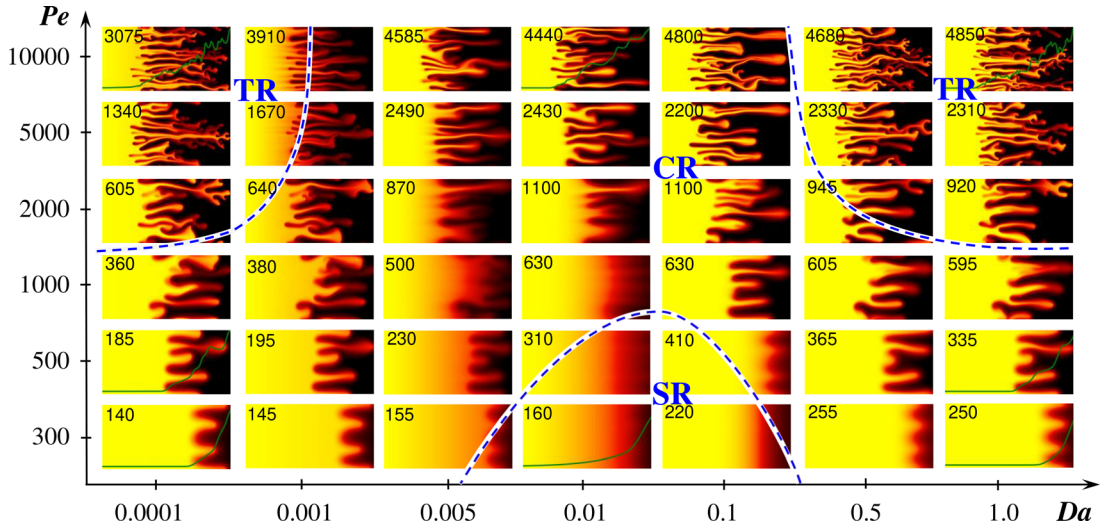


**FIG. 6.** Concentration fields in well-connected pore network $c_m$ in *Pe*–*Da* parameter space at $f = 0.6$ and $R = 3$. Dimensionless time is indicated at left top corner of each frame. Flow regimes are identified as stable regime (SR), channeling regime without tip-splitting (CR), and tip-splitting regime (TR). Note the coordinate system is not to scale. The green curves depict the *y*-averaged viscosity profiles on several representative concentration profiles in each regime. The viscosity varies spatially in the range of [1.0, $e^R$] from left to right in each frame ($R = 3.0$ in this work).

Downloaded from http://pubs.aip.org/aip/pof/article-pdf/doi/10.1063/5.0104692/16569127/092109_1_online.pdf


Published under an exclusive license by AIP Publishing

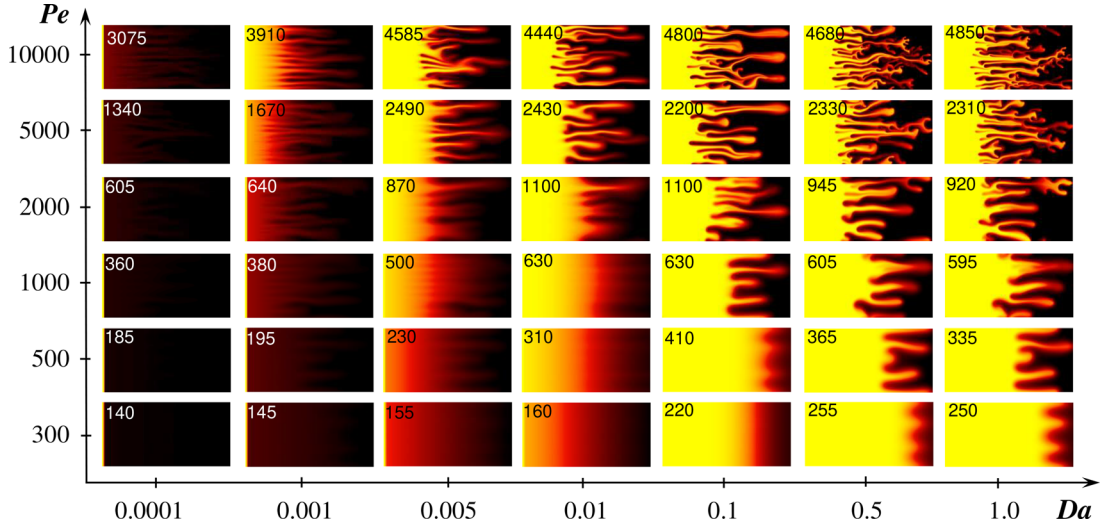


**FIG. 7.** Concentration fields in dead-end pore network $c_{im}$ in *Pe*–*Da* parameter space at $f = 0.6$ and $R = 3$. Note the coordinate system is not to scale.

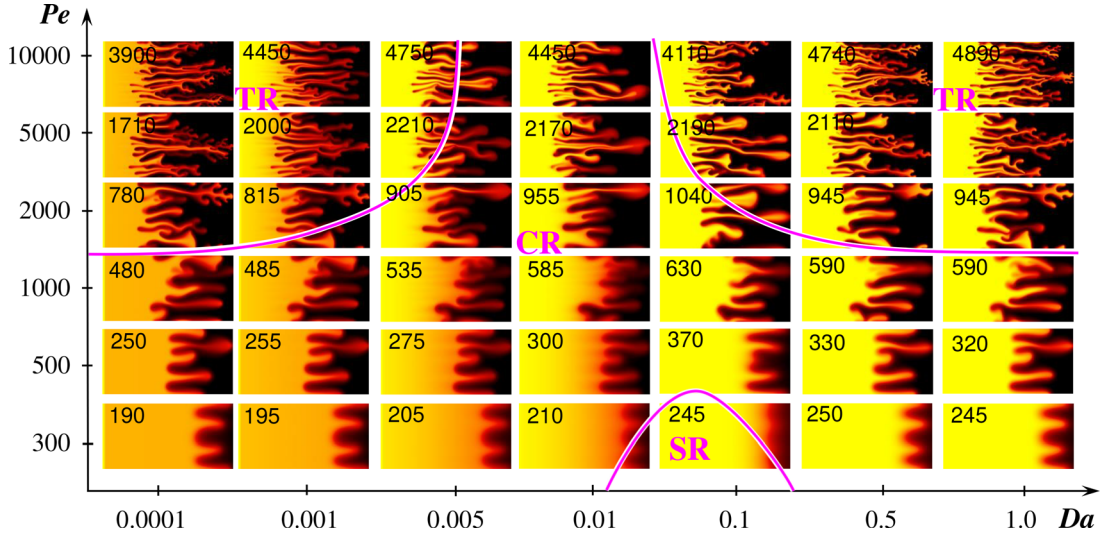


**FIG. 8.** Concentration fields $c_T$ in *Pe*–*Da* parameter space at $f = 0.8$ and $R = 3$. Note the coordinate system is not to scale.

$$\frac{\partial c_{im}}{\partial t} = \alpha T(c_m - c_{im}). \tag{C2d}$$

The order of magnitude (e.g., $\alpha T$, $DT/L^2$) in Eq. (C2) is grouped. Notice here, $L$, $U$, $T$, $C$, and $P$ can be chosen to study physical processes. For instance, potential choices for the timescale are

$$T = \left\{ T_{conv} = \frac{\phi l}{U_0}, T_{diff} = \frac{l^2}{D}, T_{pore} = \frac{1}{\alpha} \right\}, \tag{C3}$$

where $T_{conv}$, $T_{diff}$, and $T_{pore}$ are characteristic time scales for pure convective transport, diffusive transport, and immobile pore transport effects. Additionally, combinations of physical quantities that provide the same dimension may also be used via

$$L = \frac{D\phi}{U_0}, \quad U = \frac{U_0}{\phi}, \quad T = \frac{D\phi^2}{U_0^2}, \quad \text{and} \quad P = \mu_m D\phi. \tag{C4}$$

The dimensionless equations shown in Sec. III B may therefore be obtained.

## REFERENCES

[1]K. Mayfield, R. Shalliker, H. Catchpoole, A. Sweeney, V. Wong, and G. Guiochon, "Viscous fingering induced flow instability in multidimensional liquid chromatography," J. Chromatogr. A **1080**, 124–131 (2005).

[2]K.-J. Streitberger, L. Lilaj, F. Schrank, J. Braun, K.-T. Hoffmann, M. Reiss-Zimmermann, J. A. Käs, and I. Sack, "How tissue fluidity influences brain tumor progression," Proc. Natl. Acad. Sci. **117**, 128–134 (2020).

Downloaded from http://pubs.aip.org/aip/pof/article-pdf/doi/10.1063/5.0104692/16569127/092109_1_online.pdf


Published under an exclusive license by AIP Publishing

[3]M. Babaei and A. Islam, "Convective-reactive $CO_2$ dissolution in aquifers with mass transfer with immobile water," Water Resour. Res. **54**, 9585–9604, https://doi.org/10.1029/2018WR023150 (2018).
[4]N. Heinemann, J. Alcalde, J. Miocic, S. Hangx, J. Kallmeyer, C. Ostertag-Henning, A. Hassanpouryouzband, E. Thaysen, G. Strobel, C. Schmidt-Hattenberger, K. Edlmann, M. Wilkinson, M. Bentham, R. Haszeldine, R. Carbonell, and A. Rudloff, "Enabling large-scale hydrogen storage in porous media—The scientific challenges," Energy Environ. Sci. **14**, 853–864 (2021).
[5]D. Kahler and Z. Kabala, "Acceleration of groundwater remediation by deep sweeps and vortex ejections induced by rapidly pulsed pumping," Water Resour. Res. **52**, 3930–3940, https://doi.org/10.1002/2015WR017157 (2016).
[6]R. Samala, A. Chaudhuri, R. Vishnudas, J. Yeswanth, and V. Selvam, "Numerical analysis of viscous fingering and oil recovery by surfactant and polymer flooding in five-spot setup for water and oil-wet reservoirs," Geomech. Geophys. Geo-Energy Geo-Resour. **6**, 3 (2020).
[7]C. Tan and G. Homsy, "Simulation of nonlinear viscous fingering in miscible displacement," Phys. Fluids **31**, 1330–1338 (1988).
[8]F. Guo and S. Aryana, "An experimental investigation of flow regimes in imbibition and drainage using a microfluidic platform," Energies **12**, 1390 (2019).
[9]Y. Wang, S. Aryana, and M. Allen, "An extension of Darcy's law incorporating dynamic length scales," Adv. Water Resour. **129**, 70–79 (2019).
[10]Y. Wang, J. Mckinzie, F. Furtado, and S. Aryana, "Scaling analysis of two-phase flow in fractal permeability fields," Water Resour. Res. **56**, e2020WR028214, https://doi.org/10.1029/2020WR028214 (2020).
[11]N. Sabet, H. Hassanzadeh, A. D. Wit, and J. Abedi, "Scalings of Rayleigh-Taylor instability at large viscosity contrasts in porous media," Phys. Rev. Lett. **126**, 094501 (2021).
[12]M. Mishra, P. Trevelyan, C. Almarcha, and A. D. Wit, "Influence of double diffusive effects on miscible viscous fingering," Phys. Rev. Lett. **105**, 204501 (2010).
[13]A. D. Wit, "Chemo-hydrodynamic patterns and instabilities," Annu. Rev. Fluid Mech. **52**, 531–555 (2020).
[14]B. Nie, X. Liu, L. Yang, J. Meng, and X. Li, "Pore structure characterization of different rank coals using gas adsorption and scanning electron microscopy," Fuel **158**, 908–917 (2015).
[15]D. Zhao, Y. Guo, G. Wang, and X. Mao, "Characterizing nanoscale pores and its structure in coal: Experimental investigation," Energy Explor. Exploit. **37**, 1320–1347 (2019).
[16]P. Guo, "Dependency of tortuosity and permeability of porous media on directional distribution of pore voids," Transp. Porous Media **95**, 285–303 (2012).
[17]Y. Du, A. Mehmani, K. Xu, S. Kelly, M. Balhoff, and C. Torres-Verdín, "Microfluidic diagnostics of the impact of local microfracture connectivity on hydrocarbon recovery following water injection," Water Resour. Res. **55**, e2019WR026944, https://doi.org/10.1029/2019WR026944 (2020).
[18]S. Park, J. Lee, H. Yoon, and S. Shin, "Microfluidic investigation of salinity-induced oil recovery in porous media during chemical flooding," Energy Fuels **35**, 4885–4892 (2021).
[19]E. Syková and C. Nicholson, "Diffusion in brain extracellular space," Physiol. Rev. **88**, 1277–1340 (2008).
[20]Y. Sun and X. Sun, "Exploring the interstitial system in the brain: The last mile of drug delivery," Rev. Neurosci. **32**, 363–377 (2021).
[21]R. Zahn, M. F. Lagadec, and V. Wood, "Transport in lithium ion batteries: Reconciling impedance and structural analysis," ACS Energy Lett. **2**, 2452–2453 (2017).
[22]T. Nguyen, A. Demortière, B. Fleutot, B. Delobel, C. Delacourt, and S. Cooper, "The electrode tortuosity factor: Why the conventional tortuosity factor is not well suited for quantifying transport in porous Li-ion battery electrodes and what to use instead," npj Comput. Mater. **6**, 123 (2020).
[23]T. Suzuki, Y. Nakata, F. Tsutsui, and S. Tsushima, "Investigation of gas transport properties of PEMFC catalyst layers using a microfluidic device," J. Electrochem. Soc. **167**, 124519 (2020).
[24]X. Wu, Z. Xie, H. Wang, C. Zhao, D. Ng, and K. Zhang, "Improved filtration performance and antifouling properties of polyethersulfone ultrafiltration membranes by blending with carboxylic acid functionalized polysulfone," RSC Adv. **8**, 7774–7784 (2018).
[25]K. Coats and B. Smith, "Dead-end pore volume and dispersion in porous media," SPE J. **4**, 73–84 (1964).
[26]S. Shin, P. Warren, and H. Stone, "Cleaning by surfactant gradients: Particulate removal from porous materials and the significance of rinsing in laundry detergency," Phys. Rev. Appl. **9**, 034012 (2018).
[27]D. Kahler and J. Zbigniew, "Acceleration of groundwater remediation by rapidly pulsed pumping: Laboratory column tests," J. Environ. Eng. **145**, 06018009 (2019).
[28]N. Karadimitriou, V. Joekar-Niasar, M. Babaei, and C. Shore, "Critical role of the immobile zone in non-Fickian two-phase transport: A new paradigm," Environ. Sci. Technol. **50**, 4384–4392 (2016).
[29]N. Nishiyama and T. Yokoyama, "Permeability of porous media: Role of the critical pore size," J. Geophys. Res.: Solid Earth **122**, 6955–6971, https://doi.org/10.1002/2016JB013793 (2017).
[30]M. Islam and J. Azaiez, "Fully implicit finite difference pseudo-spectral method for simulating high mobility-ratio miscible displacements," Int. J. Numer. Methods Fluids **47**, 161–183 (2005).
[31]Q. Yuan, Z. Ma, J. Wang, and X. Zhou, "Influences of dead-end pores in porous media on viscous fingering instabilities and cleanup of NAPLs in miscible displacements," Water Resour. Res. **57**, e2021WR030594, https://doi.org/10.1029/2021WR030594 (2021).
[32]J. Jasti, R. Vaidya, and H. Fogler, "Capacitance effects in porous media," SPE Reservoir Eng. **3**, 1207–1214 (1988).
[33]P. Szymczak and A. Ladd, "Wormhole formation in dissolving fractures," J. Geophys. Res.: Solid Earth **114**, 1277–1340 (2009).
[34]D. Peaceman and J. H. Rachford, "The numerical solutions of parabolic and elliptic differential equations," SIAM J. **3**, 28–41 (1955).
[35]S. Lele, "Compact finite difference schemes with spectral-like resolution," J. Comput. Phys. **103**, 16–42 (1992).
[36]R. Bracewell, O. Benuman, H. Hao, and J. Villasenor, "Fast two-dimensional Hartley transform," Proc. IEEE **74**, 1282–1284 (1986).
[37]S. Salter and K. Mohanty, "Multiphase flow in porous media: I. Macroscopic observations and modelling," paper presented at the SPE Annual Technical Conference and Exhibition, New Orleans, LA, 1982.
[38]R. E. Bretz, S. L. Welch, N. R. Morrow, and F. M. Orr, "Mixing during two-phase, steady-state laboratory displacements in sandstone cores," paper presented at the SPE Annual Technical Conference and Exhibition, New Orleans, LA, 1986.
[39]L. Vargová and E. Syková, "Astrocytes and extracellular matrix in extrasynaptic volume transmission," Philos. Trans. R. Soc. London, Ser. B **369**, 1654 (2014).
[40]P. Tardy and J. Pearson, "A 1D-averaged model for stable and unstable miscible flows in porous media with varying Péclet numbers and aspect ratios," Transp. Porous Media **62**, 205–232 (2006).
[41]B. Jha, L. Cueto-Felgueroso, and R. Juanes, "Quantifying mixing in viscously unstable porous media flows," Phys. Rev. E **84**, 066312 (2011).
[42]Q. Yuan and J. Azaiez, "Miscible displacements in porous media with time-dependent injection velocities," Transp. Porous Media **104**, 57–76 (2014).
[43]X. Meng and Z. Guo, "Localized lattice Boltzmann equation model for simulating miscible viscous displacement in porous media," Int. J. Heat Mass Transfer **100**, 767–778 (2016).
[44]J. Nijjer, D. Hewitt, and J. Neufeld, "Stable and unstable miscible displacements in layered porous media," J. Fluid Mech. **869**, 468–499 (2019).
[45]T. Hota and M. Mishra, "Transient growth and symmetrizability in rectilinear miscible viscous fingering," J. Eng. Math. **120**, 111–128 (2020).
[46]A. Bonazzi, M. Morvillo, J. Im, B. Jha, and F. P. J. de Barros, "Relative impacts of permeability heterogeneity and viscosity contrast on solute mixing," Phys. Rev. Fluids **6**, 064501 (2021).
[47]R. Bretz and F. Orr, "Interpretation of miscible displacements in laboratory cores," SPE Reservoir Eng. **2**, 492–500 (1987).
[48]A. Mahmoodi, A. Javadi, and B. Sola, "Porous media acidizing simulation: New two-phase two-scale continuum modeling approach," J. Pet. Sci. Eng. **166**, 679–692 (2018).
[49]W. Brigham, "Mixing equations in short laboratory cores," SPE J. **14**, 91–99 (1974).
[50]C. Tan and G. Homsy, "Stability of miscible displacements in porous media: Rectilinear flow," Phys. Fluids **29**, 3549–3556 (1986).
[51]M. Kim and C. Choi, "The stability of miscible displacement in porous media: Nonmonotonic viscosity profiles," Phys. Fluids **23**, 084105 (2011).

Downloaded from http://pubs.aip.org/aip/pof/article-pdf/doi/10.1063/5.0104692/16569127/092109_1_online.pdf


Published under an exclusive license by AIP Publishing

[52]T. Hota, S. Pramanik, and M. Mishra, "Nonmodal linear stability analysis of miscible viscous fingering in porous media," Phys. Rev. E **92**, 053007 (2015).
[53]M. Panga, M. Ziauddin, and V. Balakotaiah, "Two-scale continuum model for simulation of wormholes in carbonate acidization," AIChE J. **51**, 3231–3248 (2005).
[54]S. Abdul Hamid and A. Muggeridge, "Fingering regimes in unstable miscible displacements," Phys. Fluids **32**, 016601 (2020).
[55]J. Batycky, B. Maini, and D. B. Fisher, "Simulation of miscible displacement in full-diameter carbonate cores," SPE J. **22**, 647–657 (1982).
[56]R. Bretz, R. Specter, and F. Orr, "Effect of pore structure on miscible displacement in laboratory cores," SPE Reservoir Eng. **3**, 857–866 (1988).
[57]I. Bahralolom, R. Bretz, and F. Orr, "Experimental investigation of the interaction of phase behavior with microscopic heterogeneity in a $CO_2$ flood," SPE Reservoir Eng. **3**, 662–672 (1988).
[58]A. Honari, B. Bijeljic, M. Johns, and E. May, "Enhanced gas recovery with $CO_2$ sequestration: The effect of medium heterogeneity on the dispersion of supercritical $CO_2$-$CH_4$," Int. J. Greenhouse Gas Control **39**, 39–50 (2015).
[59]J. Soler-Sagarra, L. Luquot, L. Martínez-Pérez, M. W. Saaltink, F. D. Gaspari, and J. Carrera, "Simulation of chemical reaction localization using a multi-porosity reactive transport approach," Int. J. Greenhouse Gas Control **48**, 59–68 (2016).
[60]W. Tian, P. Li, Y. Liu, Z. Lu, and D. Lu, "The simulation of viscous fingering by using a diffusion-limited-aggregation model during $CO_2$ flooding," J. Porous Media **21**, 483–497 (2018).
[61]S. Hrabětová and C. Nicholson, "Contribution of dead-space microdomains to tortuosity of brain extracellular space," Neurochem. Int. **45**, 467–477 (2004).
[62]R. Safford, E. Bassingthwaighte, and J. Bassingthwaighte, "Diffusion of water in cat ventricular myocardium," J. Gen. Physiol. **72**, 513–538 (1978).
[63]N. Sabet, H. Hassanzadeh, and J. Abedi, "Dynamics of viscous fingering in porous media in the presence of in situ formed precipitates and their subsequent deposition," Water Resour. Res. **56**, e2019WR027042, https://doi.org/10.1029/2019WR027042 (2020).
[64]W. Hayduk and H. Laudie, "Prediction of diffusion coefficients for nonelectrolytes in dilute aqueous solutions," AIChE J. **20**, 611–615 (1974).
[65]Z. Li, L. Yuan, G. Sun, J. Lv, and Y. Zhang, "Experimental determination of $CO_2$ diffusion coefficient in a brine-saturated core simulating reservoir condition," Energies **14**, 540 (2021).

Downloaded from http://pubs.aip.org/aip/pof/article-pdf/doi/10.1063/5.0104692/16569127/092109_1_online.pdf


Published under an exclusive license by AIP Publishing